Anisotropic and outstanding mechanical, thermal conduction, optical, and piezoelectric responses in a novel semiconducting BCN monolayer confirmed by first-principles and machine learning

Bohayra Mortazavi [a,b,*], Fazel Shojaei [c], Mehmet Yagmurcukardes [d], Alexander V. Shapeev [e], Xiaoying Zhuang [a,f,**]

[a] *Chair of Computational Science and Simulation Technology, Department of Mathematics and Physics, Leibniz Universität Hannover, Appelstraße 11, 30167, Hannover, Germany*
[b] *Cluster of Excellence PhoenixD (Photonics, Optics, and Engineering–Innovation Across Disciplines), Gottfried Wilhelm Leibniz Universität Hannover, Hannover, Germany*
[c] *Department of Chemistry, Faculty of Nano and Bioscience and Technology, Persian Gulf University, Bushehr, 75169, Iran*
[d] *Department of Photonics, Izmir Institute of Technology, Izmir, Turkey*
[e] *Skolkovo Institute of Science and Technology, Skolkovo Innovation Center, Bolshoy Bulvar, 30, Moscow, 143026, Russia*
[f] *College of Civil Engineering, Department of Geotechnical Engineering, Tongji University, 1239 Siping Road, Shanghai, China*

ARTICLE INFO

ABSTRACT

Graphene-like nanomembranes made of the neighboring elements of boron, carbon and nitrogen elements, are well-known of showing outstanding physical properties. Herein, with the aid of density functional theory (DFT) calculations, various atomic configurations of the graphene-like BCN nanosheets are investigated. DFT results reveal that depending on the atomic arrangement, the BCN monolayers may display semimetallic Dirac cone or semiconducting electronic nature. BCN nanosheets are also found to exhibit high piezoelectricity and carrier mobilities with considerable in-plane anisotropy, depending on the atomic arrangement. For the predicted most stable BCN monolayer, thermal and mechanical properties are explored using machine learning interatomic potentials. The room temperature tensile strength and lattice thermal conductivity of the most stable BCN monolayer are estimated to be orientation-dependent and remarkably high, over 78 GPa and 290 W/m.K, respectively. In addition, the thermal expansion coefficient of the monolayer BCN at room temperature is estimated to be $-3.2 \times 10^{-6} \, K^{-1}$, which is close to that of the graphene. The piezoelectric response of the herein proposed BCN lattice is also predicted to be close to that of the h-BN monolayer. Presented results highlight outstanding physics of the BCN nanosheets.

1. Introduction

Carbon in the periodic table of elements is placed between boron and nitrogen, and because of close atomic sizes and electronegativity values, can form strong covalent bonding with them. While graphene is a zero-gap semimetal, hexagonal boron-nitride (h-BN) is on contrary a famous electronic insulator. Both aforementioned nanomembranes nonetheless owing to the formation of strong covalent interactions, light-weight and highly symmetrical lattices, are able to show remarkably high mechanical strength and heat conduction properties. In other words, although h-BN and graphene show contrasting electronic natures, they both are noticeably able to show outstandingly high thermal and mechanical responses. Therefore, by keeping the native hexagonal atomic lattice, and constructing ternary lattices made of carbon, boron and nitrogen atoms, so called $h\text{-}B_xC_yN_z$, one may expect to design novel two-dimensional (2D) densely-packed covalent systems, with electronic characteristics ranging between zero-gap graphene and insulating h-BN, but yet with remarkably high thermal and mechanical properties,

comparable to those of native lattices. One major advantages of the h-$B_xC_yN_z$ 2D lattices in comparison with graphene and h-BN is that they may show appropriate narrow electronic band gaps, which is highly appealing for the applications in numerous cutting edge technologies, for many of those that neither graphene nor h-BN because of their electronic nature are suitable. In fact, various h-$B_xC_yN_z$ 2D lattices have been already fabricated. For example, BC_6N layered materials have been fabricated [1,2] and theoretical results reveal that in the single-layer form it is a semiconductor with an ability to exhibit ultrahigh heat conduction and mechanical properties [3,4]. In a latest experimental accomplishment, Seo et al. [5] succeeded in the growth of the BC_2N nanosheets via the chemical vapor deposition method. A recent theoretical study confirms that the BC_2N monolayers show also semiconducting electronic character combined with high thermal transport and mechanical properties [6].

As it is clear, h-$B_xC_yN_z$ may offer a bright possibility to design low-density, mechanically flexible and strong and highly thermally conductive 2D semiconductors [7–11]. In this work our objective is to explore the physical properties of the BCN monolayers. In this regard, in the first step various atomic configurations for the BCN monolayers are considered. In the next step density functional theory (DFT) simulations will be employed to investigate their relative energetic stability. Electronic and optical properties are subsequently analyzed to establish a connection with structural features. With the aid of first-principles calculations, the piezoelectric energy conversion of the BCN monolayers are also examined. Machine learning interatomic potentials (MLIPs) [12–15] are employed to explore the mechanical, thermal expansion and lattice thermal conductivity of the a novel BCN monolayer at room temperature. The presented theoretical results highlight highly appealing physical properties of the BCN nanosheets for the application in the next generation nanoelectronics, thermal management and energy conversion systems, very motivating for further experimental and theoretical endeavors.

2. Computational methods

DFT simulations herein were performed using the *Vienna Ab-initio Simulation Package* [16,17]. The Perdew-Burke-Ernzerhof (PBE) and generalized gradient approximation (GGA) were employed to treat the effect of exchange–correlation between the electrons. The plane wave cutoff energy was set to 500 eV with Monkhorst-Pack [18] k-point method. A vacuum spacing of 15 Å was kept between two nearest nanosheets to exclude interaction between them in the three-dimensional periodic systems. Atomic positions and simulation box sizes were relaxed until the fulfilment of the energy and force convergence of 10^{-6} eV and 0.001 eV/Å, respectively. For the geometry optimization a $15 \times 15 \times 1$ K-point grid was used. Electronic band structures were investigated by utilizing PBE/GGA and HSE06 hybrid [19] functional. The mobility of a charge carrier (electron or hole) in a defect-free semiconductor/insulator is normally dominated by the interaction of the charge carrier with acoustic phonons. Deformation potential theory (DPT), originally developed by Bardeen and Shockley [20], was used to calculate the acoustic phonon-limited charge carrier mobility within the considered BCN nanosheets. The aforementioned theory is originally formulated for isotropic materials, however because of the structural anisotropy of the considered BCN monolayers, a modified DPT version was used to take the lattice anisotropy into account. In anisotropy-corrected DPT, electron and hole mobilities along the in-plane directions (μ_{zig} and μ_{arm}) are calculated via [21–23]:

$$\mu_{zig} = \frac{5e\hbar^3 \left(5C_{zig} + 3C_{arm}\right)}{2k_b T m_{zig}^{*\frac{3}{2}} m_{arm}^{*\frac{1}{2}} \left(9E_{dzig}^2 + 7E_{dzig}E_{darm} + 4E_{darm}^2\right)} \quad (1)$$

$$\mu_{arm} = \frac{5e\hbar^3 \left(5C_{arm} + 3C_{zig}\right)}{2k_b T m_{arm}^{*\frac{3}{2}} m_{zig}^{*\frac{1}{2}} \left(9E_{darm}^2 + 7E_{darm}E_{dzig} + 4E_{dzig}^2\right)} \quad (2)$$

in which $\hbar$ is the reduced Planck constant, k_b is the Boltzmann constant, C and m^* are the elastic modulus and the effective mass, respectively, and E_d is the deformation energy constant, which mimics the charge carrier-phonons interactions for an electronic state (VBM and CBM) along the transport direction. Because of the fact that charge carrier mobilities can be further suppressed via other sources of scatterings, such as optical phonons, defects, impurities, and crystal zone boundaries, the calculated mobilities are therefore upper-bounds of experimental measurements. Density functional perturbation theory (DFPT) simulations were conducted within the VASP package to acquire phonon dispersions utilizing the PHONOPY code [24]. The optical absorption were estimated by taking the excitonic effects into consideration with the Tamm-Dancoff approximation (TDHF) via the Casida equation [25]. The absorption spectrum is subsequently calculated using the following relation:

$$\alpha(\omega) = \sqrt{2}\omega \left[\frac{\sqrt{\varepsilon_1^2 + \varepsilon_2^2} - \varepsilon_1}{2} \right]^{1/2} \quad (3)$$

Here ε_2 and ε_1 are the imaginary and real parts of the dielectric function, respectively. For the investigation of the relaxed-ion piezoelectric strain coefficients from the sum of ionic and electronic contributions, the relaxed-ion elastic stiffness tensor elements were calculated by using the small displacement methodology within the VASP package. The piezoelectric stress coefficients were obtained directly using the DFPT method with a very fine k-point mesh of $36 \times 36 \times 1$ and a considerably high plane wave kinetic energy cutoff of 700 eV. In this work we passively-fitted moment tensor potentials (MTPs) [26], utilizing the MLIP package [27] to explore the thermal and mechanical properties at finite temperatures. The required datasets for the fitting of MTPs were prepared by conducting ab-initio molecular dynamics (AIMD) simulations within the VASP package over supercells with 48 atoms, time step of 1 fs and $2 \times 2 \times 1$ K-point grid. AIMD calculations were conducted for strain-free and -4%, $+5\%$, $+10\%$ and $+14\%$ biaxially strained samples. For the strain-free sample, the temperature was gradually increased from 3 to 100 K over 800 time steps. The low temperature AIMD simulation for the unstrained sample enhances the sampling around the equilibrium conditions, which is useful for highly accurate evolution of phonon dispersion relations. For the four strained samples, during the AIMD calculations the systems were heated from 300 to 1500 K over 800 time steps. These simulations are extremely useful to enhance the stability of the potentials at high temperatures and are also required for the accurate examination of mechanical properties and capturing the failure initiation and progress. The complete AIMD trajectories were next subsampled, and around 560 configurations were used to train preliminary MTPs. The accuracy of preliminary fitted MTPs were then examined over the complete dataset, and configurations with worst extrapolation grades [28] were identified and incorporated to the original dataset. The final MTPs with enhanced accuracy and stability were then passively-fitted using the improved training dataset. Phonon dispersion relations were also obtained using the fitted MTPs employing the PHONOPY code, as explained in our earlier study [29].

Classical molecular dynamics (CMD) simulations on the basis of MTPs were conducted using the LAMMPS [30] package. For the evaluation of thermal and mechanical properties we adjusted time steps of 1.0 and 0.5 fs, respectively. Before applying the loading condition in the conducted CMD simulations, structures were equilibrated using the Nosé-Hoover barostat and thermostat method (NPT). Non-equilibrium molecular dynamics (NEMD) simulations were conducted to evaluate the length-dependent lattice thermal transport. In the NEMD approach, after the initial equilibration, few rows of atoms at the two ends were

fixed. Then, the systems along the heat transport direction were equally divided into 22 sections and a 20 K temperature difference was applied between two boundary of the models using the NVT method. The remaining part of the systems were then simulated with constant energy ensemble (NVE) simulations. The lattice thermal conductivity for a system was then obtained using the 1D Fourier's law, on the basis of the NVT imposed heat flux and the formed averaged temperature gradient along the sample's length. The thermal expansion coefficient was evaluated by gradually heating the systems consisting of 2016 atoms with a fixed 25 K step, under small in-planar stretching stresses controlled by the NPT method for 60 ps [14]. The simulation box size planar dimensions were averaged to obtain the change of the area as a function of temperature. Eight independent simulations with uncorrelated initial velocities were performed and subsequently averaged in order to find smoother relations for the thermal expansion coefficient. Mechanical properties were investigated by employing the quasi-static uniaxial tensile simulations, as that explained in our previous study [31]. In this method, the loading proceeds with a fixed strain step of 0.005, applied in every 0.1 million time increments, while the structural optimizations were performed with the NPT method to ensure uniaxial stress condition. To obtain smooth stress-strain relations, the stress values were averaged during last half of every loading step. OVITO [32] and VESTA [33] molecular packages were employed for plotting the atomic structures obtained using the CMD and DFT simulations, respectively.

3. Results and discussions

We first introduce six different considered atomic configurations for the graphene-like BCN lattices (namely BCN-n (n = 1–6), shown in Fig. 1. In this illustration, the relative energies of the BCN monolayers along with their electron localization function (ELF) [34] are also included. The structural, energetic, and electronic band gap properties of the considered BCNs are also listed in Table 1. According to the results shown in Fig. 1, herein proposed BCN-1 is the most stable configuration, which is made by covalently connected alternate segments of a single-hexagon ribbon of h-BN and a zigzag carbon chain. The in-plane bonding network of the BCN-1 is clearly anisotropic, which consequently results in anisotropy in different transport properties. Worthy to mention that according to our calculations the BCN-1 monolayer is by

Table 1
Structural, energetic, and electronic properties of the considered BCN monolayers.

System	$|\vec{a}|, |\vec{b}|$ (Å), $\gamma(°)^a$	E_{rel} (eV/atom)^b	E_{form} (eV/atom)^c	E_g^{PBE}(eV)^d	E_g^{HSE06}(eV)^e
BCN-1	2.49,6.66,79.21	0	0.167	1.84	2.46 ((H$_1$-Γ)→ (H$_1$-Γ)) 2.52 (M→M) 2.52 ((H$_2$-H$_1$)→ (H$_2$-H$_1$))
BCN-2	4.35,4.35,60	0.131	0.298	0.88	1.59 (Γ→Γ)
BCN-3	7.60,4.32,90	0.166	0.333	1.04	1.85 (Γ→Γ)
BCN-4	4.37,4.37,60	0.585	0.752	1.04	1.37 ((Γ-M)→ (Γ-M))
BCN-5	7.58,4.36, 90	0.604	0.771	0	0
BCN-6	4.38,4.38,120	0.700	0.868	0.04	0.05 ((Γ−M)→ (Γ−M))

^{a} PBE optimized lattice parameters.
^{b} Relative energy with respect to BCN-1.
^{c} Formation energy with respect to graphene and h-BN monolayers. The formation energy is defined as E_{form}= (E_{tot} (BCN-n) - m × E(C) – m × E (BN))/3 m, where Etot (BCN-n), E(C), E (BN) are total energy of BCN-n monolayer, chemical potential of a carbon atom in graphene, and chemical potential of a BN pair in h-BN, respectively and m in this formula stands for the number of BCN units in primitive cell of BCN-n monolayer.
^{d} PBE calculated band gaps.
^{e} HSE06 calculated band gaps. Band gap transition k-points are also shown in parenthesis.

1.039 eV/atom more stable than the theoretically predicted penta-BCN [35]. The BCN-2 and BCN-3 monolayers are less stable by 0.131 and 0.166 eV/atom, respectively, and they are made by parallel armchair chains of BN held together by segregated C_2 moieties. The BCN-4 and BCN-5 lattices are by approximately 0.6 eV/atom less stable configurations, and they comprise armchair chains of BC and CN and segregated N_2 and B_2 moieties, respectively. The BCN-6 is the least stable configuration, which is only made from segregated C_2, N_2, and B_2 moieties. Worth noting that the per atom energy of the BCN-1, graphene and h-BN monolayers are predicted to be −8.774, −9.225 and −8.799 eV,
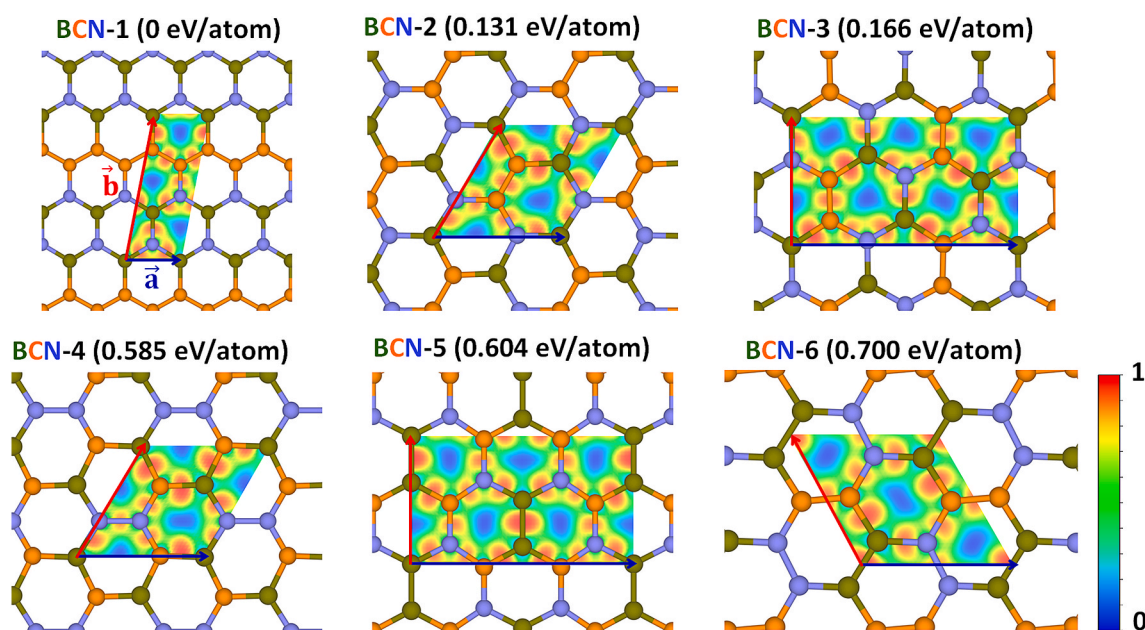

Fig. 1. Atomic configurations of the BCN monolayers along with their relative energies in eV/atom. Contours depict the ELF within the monolayers' primitive cells. (A colour version of this figure can be viewed online.)

respectively. As it is clear, a BCN structure with closer atomic configuration to the native graphene and h-BN is expected to be more stable. This is consistent with our considered BCN structures, which shows that the BCN-1 lattice with a closer atomic structure to the h-BN and graphene yields the lowest energy. In other words, the relative energetic stability data indicate that configurations with larger number of B–N and C–C bonds are more stable.

Next, the synthesis feasibility of various BCNs are investigated by calculating their formation energies (E_{form}) in comparison with graphene and h-BN (as summarized in Table 1). The formation energy for the considered BCN monolayers varies between $+0.167$ and $+0.868$ eV/atom, indicating that they are metastable with respect to the native graphene and h-BN crystals. This finding highlights that from the theoretical point of view, the most energetically stable form of the large-area BCN nanomembranes should in fact comprise covalently bonded graphene and h-BN coplanar heterostructures, which is also consistent with a latest experimental observation [36]. The positive formation energy nonetheless does not question the synthesizability of a material, otherwise bulk diamond and graphdiyne layered materials both show positive formation energies with respect to the graphite. For instance, in a combined experimental and computational study [37], the most matched graphene-like BCN monolayer, synthesized through dehydrogenation polymerization of BN cyclohexane, is found to show a formation energy of $+0.440$ eV/atom with respect to the graphene and h-BN. Taking this value as a criterion for the synthesizability of the BCNs, the BCN-1 and BCN-2 lattices with smaller formation energies as that of the

synthesized BCN [37], are also probable candidates for the experimental realization. On the other hand, being the most stable configuration of a chemical composition also does not always guarantee an easier chemical synthesis. For instance, in the above mentioned experimental-computational work [37], herein so called BCN-3 has been computationally predicted to be the global minimum structure of the polymerization process, however, a different configuration was consistent to their crystallographic data. In our previous study [6], it was also found that the recently fabricated BC_2N lattice via a rapid quenching strategy [5], is not also the global minimum structure. In Fig. 1 the ELF results are also included, which is a topological function defined between 0 and 1 [34]. Large ELF values over 0.8 appearing around the center of bonds, indicate the formation of strong covalent interactions throughout these graphene-like networks. Because of larger electronegativity of N atoms than the C and B counterparts, they tend to attract electrons from them, resulting in the formation of polar covalent bonding along the hetero bonds. In the supporting information document, the energy minimized BCN monolayers are included.

After investigating the energetic stability of various BCN monolayers, next their electronic properties will be explored. Fig. 2 shows the HSE06 band structures and projected density of states (PDOS) for the BCN-1, BCN-2 and BCN-3 monolayers, as well as only the HSE06 band structures for the other three less stable configurations. According to Fig. 2 and electronic band gap data summarized in Table 1, the considered BCN monolayers are semiconductors, except for the BCN-5 monolayer, which noticeably exhibits a semi-metallic character with a
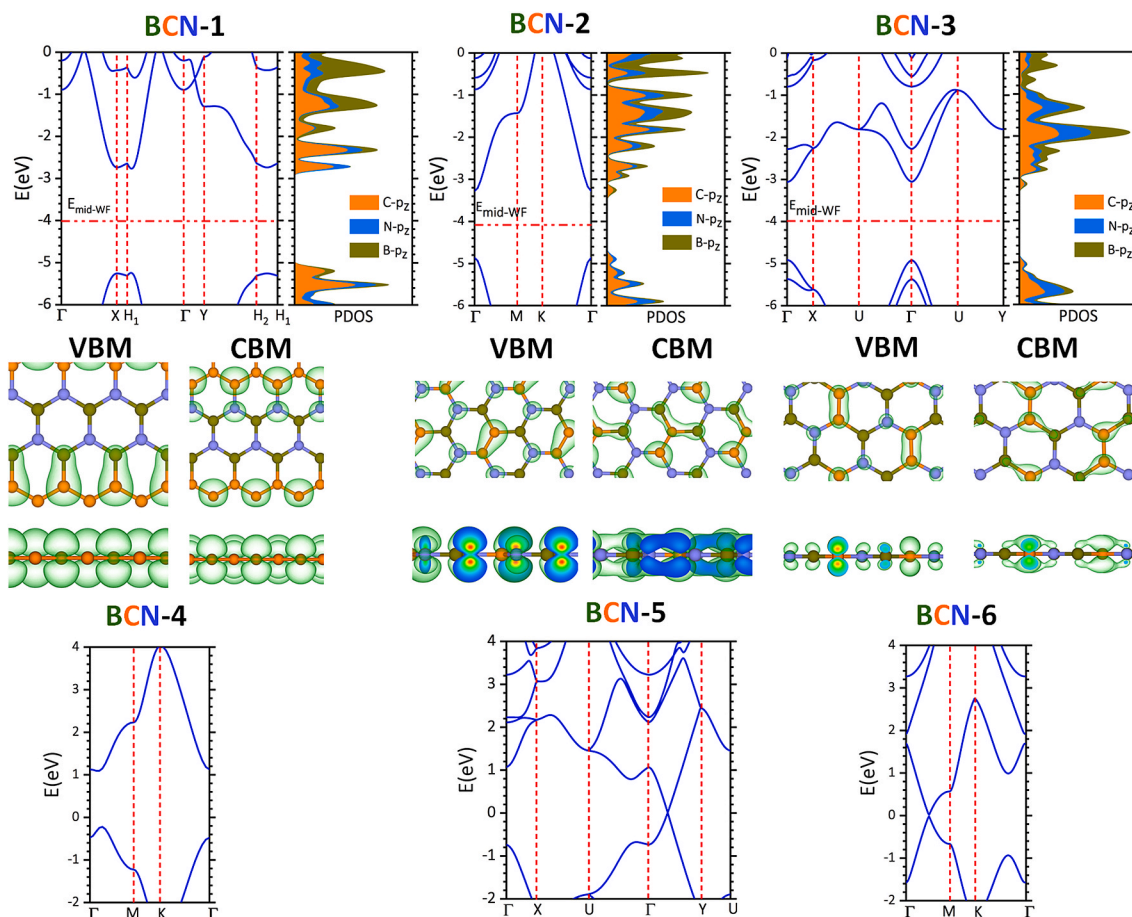

Fig. 2. HSE06 band structures and atom type- and orbital-projected density of states (PDOS), and charge density distributions at band gap transition k-points (valence band maximum (VBM) and conduction band minimum (CBM)) for the BCN-1, BCN-2 and BCN-3 monolayers, as well as corresponding band structures for the other three less stable configurations. For the HSE06 results of BCN-1, BCN-2 and BCN-3 monolayers, band energies are aligned with respect to the vacuum level and Mid-gap work functions are also mentioned. For the three less stable configurations the Fermi energy is set to 0 eV. For each lattice the first Brillouin zone and corresponding points are shown in Fig. S1. (A colour version of this figure can be viewed online.)

Dirac cone at a k-point ($0\ \vec{k_1} + 0.188\ \vec{k_2}$, where $\vec{k_1}$ and $\vec{k_2}$ are reciprocal lattice vectors of each primitive cell's Brillouin zone (BZ)) in between Γ and Y points. Among those with semiconducting character, BCN-4 possesses an indirect gap, while the other four exhibit direct gaps, which is an appealing feature for application in optics. It is also conspicuous that the band gap values are strongly dependent on the atomic configurations. The herein predicted BCN-1 monolayer shows a HSE06 (PBE) band gap of 2.46 (1.84) eV, slightly away from H_1 point of BZ toward Γ ($0.482\ \vec{k_1} + 0.241\ \vec{k_2}$). Two other slightly larger direct band gaps (~2.5 eV) are also observable in the band structure of the BCN-1 monolayer. The BCN-2 and BCN-3 monolayers both exhibit smaller HSE06 (PBE) band gaps of 1.59 (0.88) and 1.85 (1.04) eV at Γ-point of their BZ, respectively. The BCN-4 monolayer shows an even smaller band gap of 1.37 (1.04) eV, and the least stable BCN-6 counterpart yields the smallest band gap of 0.05 eV. Despite different band gaps, a glance at Fig. 2 reveal that BCN monolayers exhibit highly dispersed valence and conduction bands, implying small effective masses (find Table 2) and remarkable mobility of charge carriers. According to the PDOS and charge density distribution plots (shown in the middle panel of Fig. 2), both valence and conduction bands (VB and CB) for the BCN-1, BCN-2 and BCN-3 monolayers are contributed solely by p_z and they thus show a π-character. For the BCN-1 monolayer, VBM is distributed over B–C bonds and represents a bonding π(B–C) state, while CBM is distributed over N–C bonds with an antibonding π*(N–C) state. Both states look delocalized along the zigzag direction, explaining highly dispersed VB and CB along K to Γ. In the BCN-2 monolayer, both VBM and CBM are more delocalized and represent mostly a boding π(C–C) state and an antibonding π*(C–C) state hybridized with a bonding π(B–C) state, respectively. Although less delocalized, similar band characters as that in the BCN-2 monolayer, are consistent also for the BCN-3 system. Such delocalization of π-electrons and also small bond lengths (<1.54 Å) in the BCN-1, BCN-2 and BCN-3 monolayers lead to small effective masses and enhances the surface mobility of electron and holes.

We next employ the anisotropy-corrected version of the deformation potential theory combined with effective mass approximation in order to provide useful estimations for the carrier mobilities in the three most stable BCN-1, BCN-2 and BCN-3 monolayers, using rectangular unitcells. Table 2 summarizes the quantities involved in calculating the carrier mobilities as well as the mobility values themselves for the considered monolayers. The results summarized in Table 2 reveal that the BCN-1 and BCN-3 monolayers yield mildly anisotropic in-plane elastic values, while both configurations as well as the BCN-2 counterpart exhibit highly anisotropic effective masses and deformation potential constants, leading to different mobility values for the electrons and holes along the zigzag and armchair directions. According to our calculations, maximum electron and hole mobilities for the BCN-1 (−2, −3) monolayers at room temperature are found to be 3209 (3888, 16,605) $cm^2V^{-1}s^{-1}$ along the zigzag (armchair, zigzag) direction and 23,747 (6405, 9867) $cm^2V^{-1}s^{-1}$ along armchair (zigzag, zigzag) direction, respectively. Although these values are smaller than the experimentally reported mobility for the graphene ($2 \times 10^5\ cm^2V^{-1}s^{-1}$) [38], they are noticeably larger than those theoretically predicted for some other widely investigated 2D materials [39–42]. Table 2 also shows large differences in magnitude of electron and hole mobilities of each of the

BCN monolayers ($m_h > m_e$ for BCN-1 and BCN-2, $m_e > m_h$ for BCN-3). The remarkable difference between the electron and hole mobilities in the considered BCN monolayers is prone to enhance the efficiency of electron-hole separation, which is an appealing feature for the optoelectronic applications.

We next investigate the optical absorption of the BCN-1, BCN-2 and BCN-3 monolayers by calculating their dielectric function. Fig. 3 depicts the absorption coefficients for the light incident from the out-of-plane direction and linearly polarized along the in-plane zigzag and armchair directions. As expected the optical absorption of the BCN-1 and BCN-3 monolayers is highly anisotropic. The first absorption peaks of the BCN-1 monolayer occur at two closely lying energies of 2.56 and 2.62 eV for the zigzag and armchair polarization directions, respectively, slightly larger than our predicted band gap for this system. The absorption coefficient values of the former one ($4.3 \times 10^5\ cm^{-1}$) however are 27 times larger than that of the later one ($1.6 \times 10^4\ cm^{-1}$). For the BCN-3 monolayer, the first absorption peak for the zigzag polarization direction appears to be close to the band gap energy (1.85 eV), which is by 0.5 eV smaller than that for armchair polarization direction, indicating that this system may show mild linear dichroism. A similar, but stronger behavior has been also reported for other structurally anisotropic materials like α-phosphorene [43]. The first absorption peak of the BCN-2 monolayer also appears close to its band gap (1.59 eV). Along this monolayer generally the absorption coefficients are smaller than those of the BCN-1 and BCN-3 counterparts. The highly anisotropic optical adsorption along the BCN-1 nanosheet can be useful for the employment in the direction-dependent optoelectronic nanodevices. Presented results confirm appealing anisotropic optical characteristics of the herein predicted BCN nanosheet. In the oncoming studies, it is
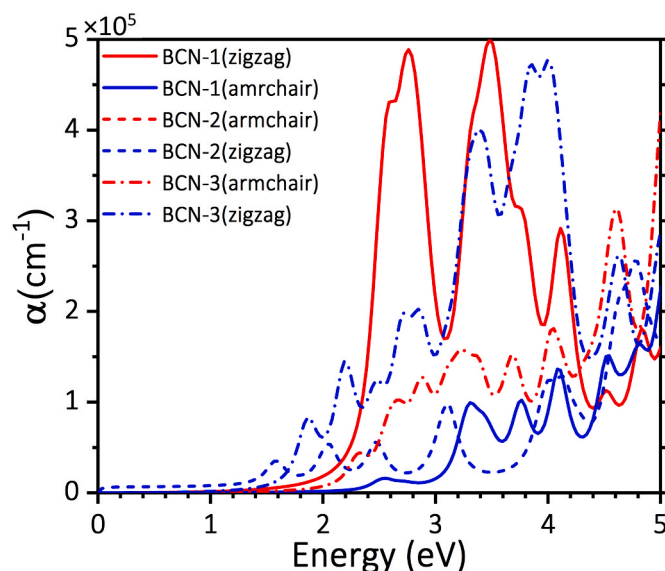

Fig. 3. Optical absorption of the BCN-1, BCN-2 and BCN-3 monolayers for the out-of-plane incidence of light, polarized along zigzag and armchair directions. (A colour version of this figure can be viewed online.)

Table 2
Calculated effective masses $|m^*|$, deformation constants E_d (eV), in-plane stiffness factors C (N/m), and carrier mobilities μ ($cm^2V^{-1}s^{-1}$) for electron (e) and hole (h) carrier types of BCN-1, BCN-2, and BCN-3 at 300 K along zigzag (zig) and armchair (arm) directions; m_0 stands for the rest mass of an electron.

Lattice	Carrier type	m_{zig}^*/m_0	m_{arm}^*/m_0	E_{dzig}	E_{darm}	C_{zig}	C_{arm}	μ_{zig}	μ_{arm}
BCN-1	e	0.24	3.10	0.90	5.80	307	300	3209	128
	h	0.32	0.11	5.20	2.11	307	300	5596	23,747
BCN-2	e	0.16	0.27	2.06	5.01	293	296	16,605	6373
	h	0.16	0.30	5.04	2.52	293	296	9867	7227
BCN-3	e	0.23	0.38	7.01	1.03	298.39	288.22	3296	3888
	h	0.22	0.43	0.32	7.93	298.39	288.22	6405	1480

thus interesting to employ a more advanced method, such as Bethe–Salpeter equation formalism to explore optical response of BCN nanosheets. Observing sizable band gaps, large and anisotropic electron and hole mobilities, and very good absorption of visible light in the BCN-1, BCN-2 and BCN-3 monolayers suggest that they might be promising candidates for application in nanoelectronics and photo-catalytic applications. We calculated the absolute band edge positions of the BCN-1, BCN-2 and BCN-3 lattices to investigate their possible application for photocatalytic water splitting. Presented data in Fig. S2 reveal that for these three monolayers, only VBMs yield proper align-ment with respect to the chemical potentials of hydrogen evolution re-action in acidic and neutral media. In a mild basic condition, however, it can be seen that band edge positions of the BCN-1 monolayer straddle the chemical potentials of both hydrogen evolution and oxygen reduc-tion reactions of water, indicating that it might be a promising candidate for photocatalytic overall water splitting.

Piezoelectric effect is the generation of electric dipole moment as a result of mechanical straining in non-centrosymmetric materials. Theoretical predictions and experimental observations have demon-strated the enhancement of piezoelectric constants in 2D materials [44, 45]. In the 2D limit, the relaxed-ion piezoelectric tensor e_{ij} can be described as the sum of ionic e_{ij}^{ion} and electronic e_{ij}^{el} contributions. The piezoelectric stress tensor e_{ij} is related to the piezoelectric strain tensor d_{ij} through the elastic stiffness tensor elements, C_{ij} as follows: $e_{ij} = d_{ik}C_{kj}$. Since calculated e_{ij} values exhibit in-plane anisotropy, one has to drive the relations along the armchair and zigzag directions. For the hexag-onal symmetry with in-plane anisotropy, the piezoelectric strain co-efficients d_{21} and d_{22} can be written as:

$$d_{21} = \frac{e_{21}C_{22} - e_{22}C_{21}}{C_{11}C_{22} - C_{21}C_{12}} \text{ and } d_{22} = \frac{e_{21}C_{12} - e_{22}C_{11}}{C_{11}C_{22} - C_{21}C_{12}} \tag{4}$$

Different from the usual in-plane isotropic hexagonal structures of graphene and MoS$_2$, the in-plane anisotropy along the armchair and zigzag directions in the herein constructed BCN monolayers should be investigated. The piezoelectricity is generated due to the non-centrosymmetric change of the dipoles in the structure. For the graphene-like BCN structures considered in this work, the in-plane anisotropy arises from the atomic arrangements. Among the six considered BCN structures, the highest piezoelectric stress tensor ele-ments are calculated for the BCN-2 system, which are 2.73×10^{-10} and 2.03×10^{-10} C/m for the e_{21} and e_{22}, respectively. Notably, these values are lower than that of the single-layer MoS$_2$ (3.7×10^{-10} C/m) [45], but very close to that of the pristine h-BN monolayer (2.9×10^{-10} C/m) [44]. Similarly, herein predicted BCN-1 monolayer is found to exhibit corresponding values of 2.00×10^{-10} and 2.60×10^{-10} C/m, respec-tively, whereas the BCN-3 structure is found to be a non-piezoelectric lattice. In addition, BCN-4 is predicted to yield 1.80×10^{-10} and 1.48×10^{-10} C/m for the e_{21} and e_{22}, respectively. The other two BCN monolayers, namely BCN-4 and BCN-6, are calculated to exhibit negli-gible piezoelectricity (0.41×10^{-10} and 0.30×10^{-10} C/m for BCN-4 and 0.21×10^{-10} and 0.19×10^{-10} C/m for BCN-6 monolayers). It is thus conspicuous that the atomic arrangement of h-B$_x$C$_y$N$_z$ significantly affect the piezoelectric properties. Moreover, the anisotropy in the piezoelectric constants arises from the atomic arrangements along the zigzag and armchair directions. For instance, the BCN-1 structure along the zigzag orientation includes two chains of B–N pairs sandwiched with zigzag C–C chains. On this basis the contribution from B–N pairs dominate the piezoelectric response due to the dipole existing between B and N atoms. In the case of BCN-3, the zigzag chains are formed by the order of bonds between C–N–B atoms, while the armchair direction is built by the atomic arrangement of C–C and B–N pairs. Since B–N pairs are aligned along the same direction, the induced dipoles also align similarly, explaining the underlying mechanism of negligible piezo-electricity along the BCN-3 monolayer.

The piezoelectric strain elements, d_{ij}, was calculated using the rela-tion mentioned earlier (Eq. (4)). The d_{21}/d_{22} values are calculated to be −1.57/−1.01, 0.58/0.81, 0/0, 0.13/−0.08, −0.73/−0.64, and 0.09/0.08 p.m./V for the BCN-1, BCN-2, BCN-3, BCN-4, BCN-5, and BCN-6 monolayers, respectively. As expected the piezoelectric strain elements display in-plane anisotropy depending on the atomic arrangement in the BCN lattices. Noticeably, the highest piezoelectric strain response is calculated for the d_{21} element of the BCN-1 structure (−1.57 p.m./V). Aforementioned finding reveals that the applied strain along the zigzag direction in the BCN-1 lattice creates the highest polarization along the armchair direction, stemmed from the charge redistribution between the B–N atoms. In contrast, the lowest response is calculated for the BCN-6 structure, in which C–C, B–B, and N–N pair arrangements results in poor charge redistribution upon an applied external strain. Nonetheless the predicted values are lower than that of the single-layer MoS$_2$ (3.8 p.m./V) [45]. Our results reveal that the atomic arrangements in the con-structed BCN structures significantly determine the piezoelectric response, arising from the alteration of charge polarizations between the constituent atoms in the lattice.

After the complete examination of optoelectronic and piezoelectric properties, we next explore the phononic thermal transport. The phonon dispersion relations of the BCN-1, BCN-2 and BCN-3 monolayers ac-quired by the DFPT method are compared in Fig. 4. Similarly to gra-phene and other h-B$_x$C$_y$N$_z$ lattices [3,6], BCN monolayers also show three acoustic modes, in which the out-of-plane mode (ZA) shows quadratic relation. As it is also clear, the ZA modes are the only phonons in these monolayers that are convincingly free of intersection with other modes, which suggest lower scattering rates along these modes. In consistency with the phonon dispersion of graphene [46], BC$_6$N [3] and BC$_2$N [6] monolayers, one may expect considerable contribution of ZA modes in the thermal transport of the BCN monolayers. As a valuable preliminary finding, the ZA acoustic mode dispersion is considerably wider along the zigzag (Γ-X) direction than the armchair (Γ-Y) coun-terpart in the BCN-1 monolayer, which reveals considerably higher phonon group velocity along the zigzag direction. This observation is reversed for the BCN-3 monolayer, however with clearly suppressed intensity. From these curves one can conclude clearly anisotropic ther-mal conductivity along the BCN-1 monolayer. For the BCN-1 mono-layer's phonon dispersion, the result on the basis of a fitted MTP are also included, which confirms an outstanding accuracy. The agreement be-tween DFPT and MTP results are excellent for the acoustic modes, which is a key requirement for the accurate examination of lattice thermal conductivity, since these modes are generally the prevailing heat car-riers in 2D crystals.

In the rest of present work, we concentrate only on the BCN-1 lattice, predicted in the current study. To evaluate the lattice thermal conduc-tivity, NEMD simulations were conducted at 300 K. One advantage of NEMD simulations is that it can take into account multi-phonon scat-terings, and is thus able to better capture the phonon transport of experimental samples. Although MTPs are already proven to outperform the classical counterparts in the accurate evaluation of thermal transport [3,6,46], but their computational costs are by around two orders of magnitude higher than those based on the empirical Tersoff potential. Therefore, it is insightful to also evaluate thermal conductivity with popular empirical interatomic potentials. The optimized Tersoff [47] potential proposed by Lindsay and Broido [48] is currently the most accurate choice [49–51] for the simulation of thermal conductivity of graphene and other 2D carbon materials. As a highly popular approach [52–57], the Tersoff potentials developed by Kinaci et al. [58] and Lindsay and Broido [59] for the h-BN are mixed with the original opti-mized Tersoff [47] to simulate the h-B$_x$C$_y$N$_z$ lattices. Since in the NEMD simulations of heat conduction, the atoms at the two ends are fixed, the contribution of long wavelength phonons become restricted and thus the effects of length on the lattice thermal conductivity is ought to be examined. As a well-stablished approach, based on the NEMD pre-dictions for the samples with finite lengths of L, κ_L, the diffusive pho-nonic thermal conductivity, κ_∞, and phonon mean free path, Λ, can be estimated by Ref. [60]:
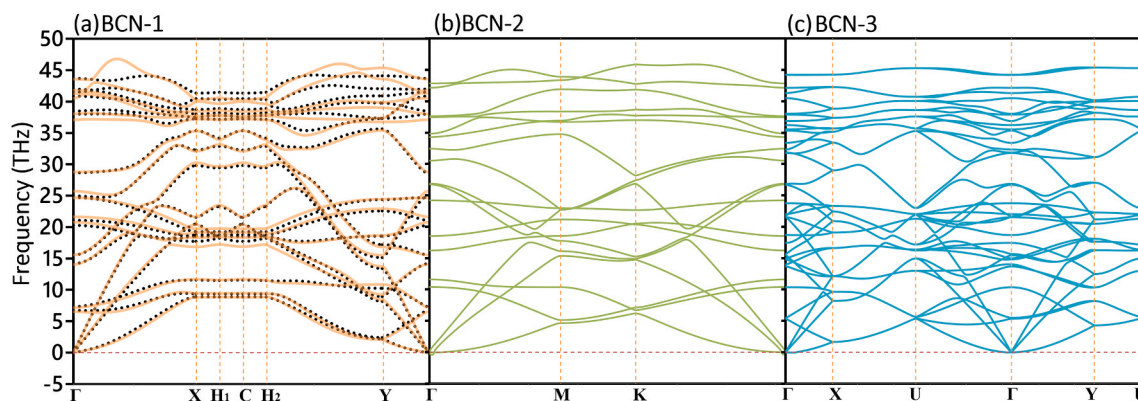
Fig. 4. Phonon dispersion of the BCN-1, BCN-2 and BCN-3 monolayers acquired by the DFPT method. The dotted lines for the BCN-1 are the predictions on the basis of the fitted MTP potential. (A colour version of this figure can be viewed online.)

$$\frac{1}{\kappa_L} = \frac{1}{\kappa_\infty}\left(1+\frac{\Lambda}{L}\right) \tag{5}$$

In Fig. 5, the NEMD results for the length and direction effect on the lattice thermal conductivity of the BCN-1 monolayer at room temperature are plotted. Using the MTP-based models, the diffusive thermal conductivity of the BCN-1 monolayer along the zigzag and armchair directions are predicted to be 416 and 293 ± 20 W/m.K, respectively. As it is clear from the results illustrated in Fig. 5, the developed classical models despite of around two orders of magnitude accelerated computational costs, considerably overestimate the MTP-based results, particularly along the zigzag direction. While it was previously found [3] that the Tersoff potentials by Lindsay and Broido [59] yields a higher accuracy for the modeling of thermal transport along the BC_6N monolayer, that proposed by Kinaci et al. [58] is clearly superior for studying the BCN and BC_2N [6] monolayers. Using the Tersoff potential proposed by Lindsay and Broido [59] for the h-BN monolayer, the room temperature thermal conductivity was predicted to be around 600 W/m.K [61]. Interestingly, with the incorporation of zigzag carbon chains, both considered Tersoff potentials show slightly enhanced thermal transport along the zigzag direction in the BCN-1 monolayer than the pristine h-BN counterpart. With the first-principles MTP-based calculations, the incorporation of carbon chains in the h-BN lattice is found to act more as a source of phonon scattering, which is consistent with phonon dispersion relation presented earlier. In a sharp contrast, with the empirical interatomic potentials, carbon chains are found to even slightly enhance the thermal transport along the zigzag direction. It is thus clear that the employed popular empirical interatomic potentials not only fail to accurately reproduce the phononic thermal conductivity values of the

h-$B_xC_yN_z$ lattices, but may also misrepresent the underlying physics.

It is also useful to study the thermal expansion of the BCN-1 monolayer using the developed accurate MTP model. Thermal expansion is evaluated using the $\frac{1}{A}\frac{dA}{dT}$ relation, where A is the projected area of the BCN-1 monolayer. The projected area was simply calculated using the in-plane simulation box values. By fitting a polynomial curve to the molecular dynamics projected area data points over eight independent calculations, the thermal expansion of the BCN-1 monolayer as a function of temperature [14,62] was acquired, which is presented in Fig. 6.
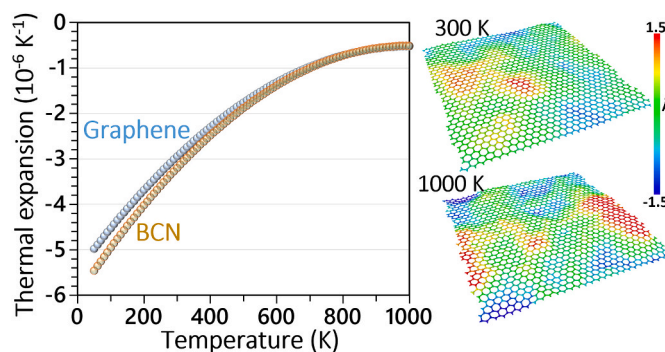

Fig. 6. Thermal expansion coefficient of the BCN-1 and graphene monolayers as a function of temperature. Right panels illustrate the atomic configuration at 300 and 1000 K, in which color coding shows the out-of-plane displacement of atoms with respect to the monolayer's center of mass. (A colour version of this figure can be viewed online.)
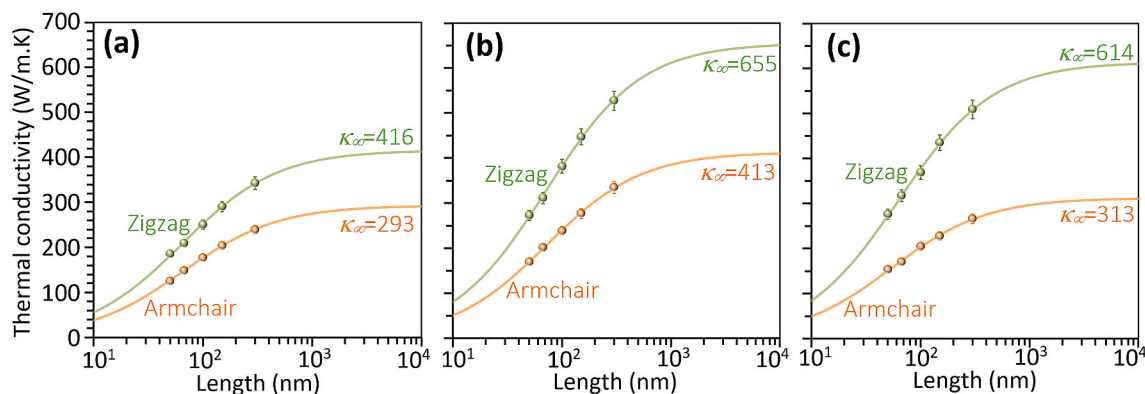

Fig. 5. NEMD results for the length and direction effect on the room temperature phononic thermal conductivity of the BCN-1 monolayer, on the basis of (a) MTP and Tersoff potentials by (b) Lindsay and Broido [59] and (c) Kinaci et al. [58]. The solid lines are fitted curves to find diffusive lattice thermal conductivity, k_∞. (A colour version of this figure can be viewed online.)

For a better insight, the corresponding curve for graphene [14] is also included. The thermal expansion coefficient of the BCN-1 monolayer at room temperature is predicted to be -3.2×10^{-6} K^{-1}, which is considerably close to that of the graphene, -2.95×10^{-6} K^{-1} [14,62]. Despite different chemical composition of the BCN-1 monolayer, its thermal expansion shows close values to graphene, which can be attributed to similar atomic structure and close stiffness values. In consistency with other graphene-like lattices [14], and also as it is shown in Fig. 6, by increasing the temperature as a result of formation of out-of-plane wrinkles the projected area decreases, resulting in a fairly high negative thermal expansion along the BCN-1 monolayer.

Last but not the least, we investigate the mechanical response of the BCN-1 monolayer by the MTP-based model and compare the results with DFT method to evaluate the accuracy of the developed classical model. In this case, in order to be closer to the results on the basis of ground-state DFT, the temperature of molecular dynamics simulations was set at 1 K, using the NPT method. In Fig. 7, the predicted uniaxial stress-strain responses of the BCN-1 monolayer along the armchair and zigzag directions, by the MTP and DFT methods are compared. In these results, real volumes of the deformed lattices are considered in the conversion of the stress values to the standard GPa unit. The real volume of the deformed BCN-1 monolayer was obtained using the simulation box sizes along the in-plane directions multiplied by a constant thickness of 3.35 Å. Plotted stress-strain curves in Fig. 7 are uniaxial, which means that during the complete deformation and after the structural relaxation the stretched BCN-1 monolayer exhibits stress component only along the loading direction and preserves negligible values along the two other perpendicular directions. In accordance with our findings for the phonon dispersion relations, it is noticeable that the predicted stress-strain curves by the MTP model agree closely with those with the ground-state DFT. The ultimate tensile strength of the BCN-1 monolayer along the armchair and zigzag directions by the DFT method are predicted to be 81.9 and 105.5 GPa, respectively, which are considerably close to the predicted values of 82.2 and 100.0 GPa by the MTP model, respectively. These results confirm that the trainedclassical model could very precisely reproduce the effect of loading direction on the mechanical response of the BCN-1 monolayer. We finally investigate the mechanical properties at 300 K using large systems with 960 atoms, which are computationally infeasible to be examined by the DFT method. In Fig. 7c, the predicted tensile behavior of the BCN-1 monolayer at 300 K are illustrated. The ultimate tensile strength of the BCN-1 monolayer along the armchair and zigzag directions at 300 K are predicted to be 78 and 93 GPa, respectively, which are by around 7% suppressed than those predicted at 1 K. These results reveal remarkably high tensile strength of the predicted BCN-1 lattice in this work.

4. Concluding remarks

In this work, first-principles calculations were carried out to investigate various atomic configurations for the graphene-like BCN nanosheets. The structures are referred according to their energetic stability, BCN-n, in which a lattice with a higher "n" is energetically less stable. The relative stability data of the six considered configurations confirm that lattices with larger number of B–N and C–C bonds yield higher energetic stability. From the theoretical point of view, it is found that most stable large-area BCN nanosheets should comprise covalently bonded graphene and h-BN coplanar heterostructures and it was thus concluded that the considered BCN monolayers are metastable. Because of the fact that the calculated formation energies from the BCN-1 to BCN-3 nanosheets are shown to be less positive than that of an experimentally realized BCN configuration, considered BCN lattices are nonetheless found as viable candidates for the experimental realization. Our results revealed that all of the considered BCN monolayers are semiconductors with electronic band gaps varying from 0.05 to 2.46 eV, except one lattice which noticeably exhibits a semi-metallic character with a Dirac cone. Our predicted most stable monolayer, namely BCN-1, was found to show largely different carrier mobilities for the electrons and holes along zigzag and armchair directions. Maximum mobility at room temperature for this lattice is predicted to be 23,747 cm^{2}V^{-1}s^{-1}, which is remarkably high. The anisotropy in the atomic structure of the BCN-1 is also reflected in highly anisotropic optical absorption, promising for applications in angle-dependent optical systems. The BCN-1 lattice is also found to be a promising nanomaterial for piezoelectric energy conversion and might be also appealing for photocatalytic overall water splitting. Moment tensor potentials (MTPs) were passively fitted to investigate the mechanical, thermal expansion and lattice thermal conductivity of the BCN-1 monolayer at room temperature. Comparison between the DFT and MTP-based results for the phonon dispersion relations and stress-strain curves close to the ground state confirm the outstanding accuracy of the developed classical models. The tensile strength and thermal conductivity of the BCN-1 monolayer at room temperature were estimated to be directionally dependent and remarkably high, over 78 GPa and 290 W/m.K, respectively. This study provides a useful vision concerning the energetic stability and physical properties of the considered BCN nanosheets. We moreover predicted a novel direct-gap semiconducting BCN lattice with anisotropic and remarkably high mechanical strength, heat conduction, carrier mobility and piezoelectric properties.

CRediT authorship contribution statement

Bohayra Mortazavi: Conceptualization, Data curation, Formal analysis, Investigation, Methodology, Resources, Software, Validation, Writing – original draft, Writing – review & editing. **Fazel Shojaei:**
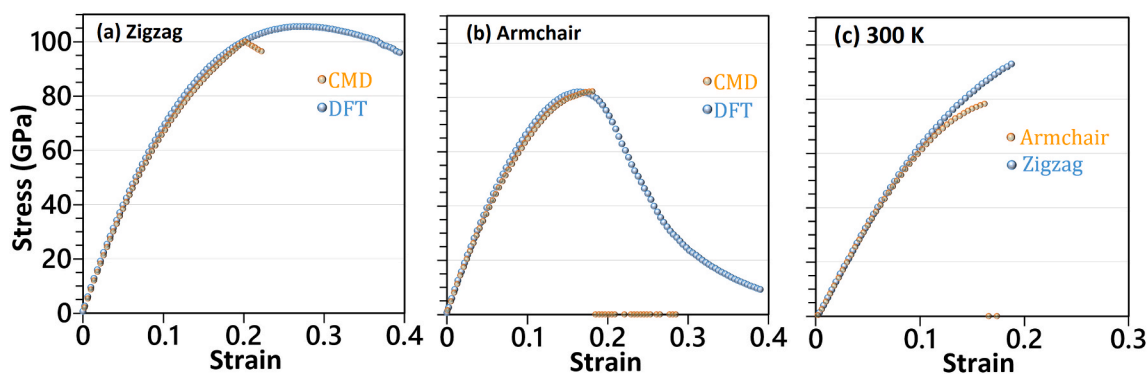

Fig. 7. Predicted uniaxial stress-strain responses of the BCN-1 monolayer along the (a) zigzag and (b) armchair directions by DFT and MTP-based molecular dynamics simulations carried out at 1 K. (c) MTP-based uniaxial stress-strain response of the BCN-1 monolayer at 300 K. (A colour version of this figure can be viewed online.)

Declaration of competing interest

The authors declare that they have no known competing financial interests or personal relationships that could have appeared to influence the work reported in this paper.

Acknowledgment

Appendix. ASupplementary data

Supplementary data to this article can be found online at https://doi.org/10.1016/j.carbon.2022.08.077.

References

[1] M. Kawaguchi, Y. Imai, N. Kadowaki, Intercalation chemistry of graphite-like layered material BC6N for anode of Li ion battery, J. Phys. Chem. Solids. 67 (2006) 1084–1090, https://doi.org/10.1016/j.jpcs.2006.01.036.

[2] M. Kawaguchi, Y. Wakukawa, T. Kawano, Preparation and electronic state of graphite-like layered material BC6N, Synth. Met. 125 (2001) 259–263, https://doi.org/10.1016/S0379-6779(01)00540-9.

[3] B. Mortazavi, Ultrahigh thermal conductivity and strength in direct-gap semiconducting graphene-like BC6N: a first-principles and classical investigation, Carbon N. Y. 182 (2021) 373–383, https://doi.org/10.1016/j.carbon.2021.06.038.

[4] B. Mortazavi, M. Shahrokhi, M. Raeisi, X. Zhuang, L.F.C. Pereira, T. Rabczuk, Outstanding strength, optical characteristics and thermal conductivity of graphene-like BC3 and BC6N semiconductors, Carbon N. Y. 149 (2019) 733–742, https://doi.org/10.1016/j.carbon.2019.04.084.

[5] T.H. Seo, W. Lee, K.S. Lee, J.Y. Hwang, D.I. Son, S. Ahn, H. Cho, M.J. Kim, Dominant formation of h-BC2N in h-BxCyNz films: CVD synthesis and characterization, Carbon N. Y. 182 (2021) 791–798, https://doi.org/10.1016/j.carbon.2021.06.080.

[6] B. Mortazavi, I.S. Novikov, A. V Shapeev, A machine-learning-based investigation on the mechanical/failure response and thermal conductivity of semiconducting BC2N monolayers, Carbon N. Y. 188 (2022) 431–441, https://doi.org/10.1016/j.carbon.2021.12.039.

[7] R. Bahadur, G. Singh, Y. Bando, A. Vinu, Advanced porous borocarbonitride nanoarchitectonics: their structural designs and applications, Carbon N. Y. 190 (2022) 142–169, https://doi.org/10.1016/j.carbon.2021.01.013.

[8] J.-H. Wee, K. Nomura, H. Nishihara, D.-W. Kim, S. Hong, G.B. Choi, S.Y. Yeo, J. H. Kim, H.-Y. Jung, Y.A. Kim, Edgeless porous carbon coating for durable and powerful lead-carbon batteries, Carbon N. Y. 185 (2021) 419–427, https://doi.org/10.1016/j.carbon.2021.09.046.

[9] V. Meunier, C. Ania, A. Bianco, Y. Chen, G.B. Choi, Y.A. Kim, N. Koratkar, C. Liu, J. M.D. Tascon, M. Terrones, Carbon science perspective in 2022: current research and future challenges, Carbon N. Y. 195 (2022) 272–291, https://doi.org/10.1016/j.carbon.2022.04.015.

[10] S. Hong, J. Nam, S. Park, D. Lee, M. Park, D.S. Lee, N.D. Kim, D.-Y. Kim, B.-C. Ku, Y.A. Kim, J.Y. Hwang, Carbon nanotube fibers with high specific electrical conductivity: synergistic effect of heteroatom doping and densification, Carbon N. Y. 184 (2021) 207–213, https://doi.org/10.1016/j.carbon.2021.08.024.

[11] Y. Su, S. Cao, L.-B. Shi, P. Qian, Investigation of biaxial strain behavior and phonon-limited mobility for γ graphyne: first-principles calculation, J. Appl. Phys. 130 (2021), 195703, https://doi.org/10.1063/5.0065325.

[12] S. Arabha, Z.S. Aghbolagh, K. Ghorbani, M. Hatam-Lee, A. Rajabpour, Recent advances in lattice thermal conductivity calculation using machine-learning interatomic potentials, J. Appl. Phys. 130 (2021), 210903, https://doi.org/10.1063/5.0069443.

[13] B. Javvaji, B. Mortazavi, X. Zhuang, T. Rabczuk, Exploring tensile piezoelectricity and bending flexoelectricity of diamane monolayers by machine learning, Carbon N. Y. 185 (2021) 558–567, https://doi.org/10.1016/j.carbon.2021.09.007.

[14] B. Mortazavi, A. Rajabpour, X. Zhuang, T. Rabczuk, A. V Shapeev, Exploring thermal expansion of carbon-based nanosheets by machine-learning interatomic potentials, Carbon N. Y. 186 (2022) 501–508, https://doi.org/10.1016/j.carbon.2021.10.059.

[15] B. Mortazavi, F. Shojaei, M. Shahrokhi, M. Azizi, T. Rabczuk, A.V. Shapeev, X. Zhuang, Nanoporous C3N4, C3N5 and C3N6 nanosheets; novel strong semiconductors with low thermal conductivities and appealing optical/electronic properties, Carbon N. Y. 167 (2020) 40–50, https://doi.org/10.1016/j.carbon.2020.05.105.

[16] G. Kresse, J. Furthmüller, Efficient iterative schemes for ab initio total-energy calculations using a plane-wave basis set, Phys. Rev. B. 54 (1996) 11169–11186, https://doi.org/10.1103/PhysRevB.54.11169.

[17] J.P. Perdew, K. Burke, M. Ernzerhof, Generalized gradient approximation made simple, Phys. Rev. Lett. 77 (1996) 3865–3868, https://doi.org/10.1103/PhysRevLett.77.3865.

[18] H. Monkhorst, J. Pack, Special points for Brillouin zone integrations, Phys. Rev. B. 13 (1976) 5188–5192, https://doi.org/10.1103/PhysRevB.13.5188.

[19] A.V. Krukau, O.A. Vydrov, A.F. Izmaylov, G.E. Scuseria, Influence of the exchange screening parameter on the performance of screened hybrid functionals, J. Chem. Phys. 125 (2006), 224106, https://doi.org/10.1063/1.2404663.

[20] J. Bardeen, W. Shockley, Deformation potentials and mobilities in non-polar crystals, Phys. Rev. 72 (1950) 80, https://doi.org/10.1103/PhysRev.80.72.

[21] H. Lang, S. Zhang, Z. Liu, Mobility anisotropy of two-dimensional semiconductors, Phys. Rev. B. 94 (2016), 235306, https://doi.org/10.1103/PhysRevB.94.235306.

[22] M. Zhou, X. Chen, M. Li, A. Du, Widely tunable and anisotropic charge carrier mobility in monolayer tin(<scp>ii</scp>) selenide using biaxial strain: a first-principles study, J. Mater. Chem. C. 5 (2017) 1247–1254, https://doi.org/10.1039/C6TC04692D.

[23] Y. Su, S. Cao, L.-B. Shi, P. Qian, Investigation of strain behavior and carrier mobility of organic–inorganic hybrid perovskites: (C 4 H 9 NH 3) 2 GeI 4 and (C 4 H 9 NH 3) 2 SnI 4, Nanoscale 12 (2020) 22551–22563, https://doi.org/10.1039/D0NR06405J.

[24] A. Togo, I. Tanaka, First principles phonon calculations in materials science, Scr. Mater. 108 (2015) 1–5, https://doi.org/10.1016/j.scriptamat.2015.07.021.

[25] T. Sander, E. Maggio, G. Kresse, Beyond the Tamm-Dancoff approximation for extended systems using exact diagonalization, Phys. Rev. B. 92 (2015), 45209, https://doi.org/10.1103/PhysRevB.92.045209.

[26] A.V. Shapeev, Moment tensor potentials: a class of systematically improvable interatomic potentials, Multiscale Model. Simul. 14 (2016) 1153–1173, https://doi.org/10.1137/15M1054183.

[27] A.S. Ivan Novikov, Konstantin Gubaev, Evgeny Podryabinkin, The MLIP package: moment tensor potentials with MPI and active learning, Mach. Learn. Sci. Technol. 2 (2021), 025002. http://iopscience.iop.org/article/10.1088/2632-2153/abc9fe.

[28] E. V Podryabinkin, A. V Shapeev, Active learning of linearly parametrized interatomic potentials, Comput. Mater. Sci. 140 (2017) 171–180, https://doi.org/10.1016/j.commatsci.2017.08.031.

[29] B. Mortazavi, I.S. Novikov, E. V Podryabinkin, S. Roche, T. Rabczuk, A. V Shapeev, X. Zhuang, Exploring phononic properties of two-dimensional materials using machine learning interatomic potentials, Appl. Mater. Today. 20 (2020), 100685, https://doi.org/10.1016/j.apmt.2020.100685.

[30] S. Plimpton, Fast parallel algorithms for short-range molecular dynamics, J. Comput. Phys. 117 (1995) 1–19, https://doi.org/10.1006/jcph.1995.1039.

[31] B. Mortazavi, M. Silani, E. V Podryabinkin, T. Rabczuk, X. Zhuang, A. V Shapeev, First-principles multiscale modeling of mechanical properties in graphene/borophene heterostructures empowered by machine-learning interatomic potentials, Adv. Mater. 33 (2021), 2102807, https://doi.org/10.1002/adma.202102807.

[32] A. Stukowski, Visualization and analysis of atomistic simulation data with OVITO–the Open Visualization Tool, Model. Simul. Mater. Sci. Eng. 18 (2009), 015012, https://doi.org/10.1088/0965-0393/18/1/015012.

[33] K. Momma, F. Izumi, VESTA 3 for three-dimensional visualization of crystal, volumetric and morphology data, J. Appl. Crystallogr. 44 (2011) 1272–1276, https://doi.org/10.1107/S0021889811038970.

[34] B. Silvi, A. Savin, Classification of chemical-bonds based on topological analysis of electron localization functions, Nature 371 (1994) 683–686, https://doi.org/10.1038/371683a0.

[35] K. Zhao, Y. Guo, Y. Shen, Q. Wang, Y. Kawazoe, P. Jena, Penta-BCN: a new ternary pentagonal monolayer with intrinsic piezoelectricity, J. Phys. Chem. Lett. 11 (2020) 3501–3506, https://doi.org/10.1021/acs.jpclett.0c00824.

[36] N. Herrera-Reinoza, A.C. dos Santos, L.H. de Lima, R. Landers, A. de Siervo, Atomically precise bottom-up synthesis of h-BNC: graphene doped with h-BN nanoclusters, Chem. Mater. 33 (2021) 2871–2882, https://doi.org/10.1021/acs.chemmater.1c00081.

[37] S. Beniwal, J. Hooper, D.P. Miller, P.S. Costa, G. Chen, S.-Y. Liu, P.A. Dowben, E.C. H. Sykes, E. Zurek, A. Enders, Graphene-like boron–carbon–nitrogen monolayers, ACS Nano 11 (2017) 2486–2493, https://doi.org/10.1021/acsnano.6b08136.

[38] K.I. Bolotin, K.J. Sikes, Z. Jiang, M. Klima, G. Fudenberg, J. Hone, P. Kim, H. L. Stormer, Ultrahigh electron mobility in suspended graphene, Solid State Commun 146 (2008) 351–355, https://doi.org/10.1016/J.SSC.2008.02.024.

[39] S.H. Mir, V.K. Yadav, J.K. Singh, Recent advances in the carrier mobility of two-dimensional materials: a theoretical perspective, ACS Omega 5 (2020) 14203–14211, https://doi.org/10.1021/acsomega.0c01676.

[40] Y. Su, N. Li, L.-B. Shi, Y.-Z. Wang, P. Qian, Investigation of carrier transport behavior for cubic CH3NH3SnX3 and CH3NH3PbX3 (X=Br and I) using Boltzmann transport equation, Comput. Mater. Sci. 213 (2022), 111609, https://doi.org/10.1016/j.commatsci.2022.111609.

[41] Y. Zhang, S. Cao, Y. Wang, X. Jian, L. Shi, P. Qian, Theoretical prediction of intrinsic carrier mobility of monolayer C7N6: first-principles study, Phys. Lett. A. 401 (2021), 127340, https://doi.org/10.1016/j.physleta.2021.127340.

[42] L.-B. Shi, Y.-Y. Zhang, X.-M. Xiu, H.-K. Dong, Structural characteristics and strain behavior of two-dimensional C3N : first principles calculations, Carbon N. Y. 134 (2018) 103–111, https://doi.org/10.1016/j.carbon.2018.03.076.

[43] J. Qiao, X. Kong, Z.-X. Hu, F. Yang, W. Ji, High-mobility transport anisotropy and linear dichroism in few-layer black phosphorus, Nat. Commun. 5 (2014) 4475, https://doi.org/10.1038/ncomms5475.

[44] P. Ares, T. Cea, M. Holwill, Y.B. Wang, R. Roldán, F. Guinea, D. V Andreeva, L. Fumagalli, K.S. Novoselov, C.R. Woods, Piezoelectricity in monolayer hexagonal boron nitride, Adv. Mater. 32 (2020), 1905504, https://doi.org/10.1002/adma.201905504.

[45] M. Yagmurcukardes, C. Sevik, F.M. Peeters, Electronic, vibrational, elastic, and piezoelectric properties of monolayer Janus MoSTe phases: a first-principles study, Phys. Rev. B. 100 (2019), 45415, https://doi.org/10.1103/PhysRevB.100.045415.

[46] B. Mortazavi, E. V Podryabinkin, S. Roche, T. Rabczuk, X. Zhuang, A. V Shapeev, Machine-learning interatomic potentials enable first-principles multiscale modeling of lattice thermal conductivity in graphene/borophene heterostructures, Mater. Horizons. 7 (2020) 2359–2367, https://doi.org/10.1039/D0MH00787K.

[47] J. Tersoff, Empirical interatomic potential for carbon, with applications to amorphous carbon, Phys. Rev. Lett. 61 (1988) 2879–2882, https://doi.org/10.1103/PhysRevLett.61.2879.

[48] B. Lindsay, Optimized Tersoff and Brenner empirical potential parameters for lattice dynamics and phonon thermal transport in carbon nanotubes and graphene, Phys. Rev. B - Condens. Matter Mater. Phys. 82 (2010), 205441.

[49] Z. Fan, L.F.C. Pereira, H.-Q. Wang, J.-C. Zheng, D. Donadio, A. Harju, Force and heat current formulas for many-body potentials in molecular dynamics simulations with applications to thermal conductivity calculations, Phys. Rev. B. 92 (2015), 94301, https://doi.org/10.1103/PhysRevB.92.094301.

[50] P. Ying, T. Liang, Y. Du, J. Zhang, X. Zeng, Z. Zhong, Thermal transport in planar sp2-hybridized carbon allotropes: a comparative study of biphenylene network, pentaheptite and graphene, Int. J. Heat Mass Transf. 183 (2022), 122060, https://doi.org/10.1016/j.ijheatmasstransfer.2021.122060.

[51] L.F.C. Pereira, Investigating mechanical properties and thermal conductivity of 2D carbon-based materials by computational experiments, Comput. Mater. Sci. 196 (2021), 110493, https://doi.org/10.1016/j.commatsci.2021.110493.

[52] A.E. Senturk, Exploring the interfacial thermal resistance and mechanical properties of hybrid C3N–BC3, Appl. Phys. A 128 (2022) 638, https://doi.org/10.1007/s00339-022-05782-9.

[53] A.E. Senturk, Outstanding thermo-mechanical properties of graphene-like B3C3 and C3N3, Appl. Phys. A. 126 (2020) 584, https://doi.org/10.1007/s00339-020-03764-3.

[54] A.E. Senturk, Thermo-mechanical properties of different structures of BC2N, Mol. Simul. (2021) 1–9, https://doi.org/10.1080/08927022.2021.1986221.

[55] S.M. Hatam-Lee, A. Rajabpour, S. Volz, Thermal conductivity of graphene polymorphs and compounds: from C3N to graphdiyne lattices, Carbon N. Y. 161 (2020) 816–826, https://doi.org/10.1016/j.carbon.2020.02.007.

[56] A. Rajabpour, S. Bazrafshan, S. Volz, Carbon-nitride 2D nanostructures: thermal conductivity and interfacial thermal conductance with the silica substrate, Phys. Chem. Chem. Phys. 21 (2019) 2507–2512, https://doi.org/10.1039/C8CP06992A.

[57] S. Sadeghzadeh, Effects of vacancies and divacancies on the failure of C3N nanosheets, Diam. Relat. Mater. 89 (2018) 257–265, https://doi.org/10.1016/J.DIAMOND.2018.09.018.

[58] A. KInacI, J.B. Haskins, C. Sevik, T. ÇaĞIn, Thermal conductivity of BN-C nanostructures, Phys. Rev. B - Condens. Matter Mater. Phys. 86 (2012), 115410, https://doi.org/10.1103/PhysRevB.86.115410.

[59] L. Lindsay, D.A. Broido, Enhanced thermal conductivity and isotope effect in single-layer hexagonal boron nitride, Phys. Rev. B. 84 (2011), 155421, https://doi.org/10.1103/PhysRevB.84.155421.

[60] P.K. Schelling, S.R. Phillpot, P. Keblinski, Comparison of atomic-level simulation methods for computing thermal conductivity, Phys. Rev. B. 65 (2002) 1–12, https://doi.org/10.1103/PhysRevB.65.144306.

[61] B. Mortazavi, T. Rabczuk, Multiscale modeling of heat conduction in graphene laminates, Carbon N. Y. 85 (2015) 1–7, https://doi.org/10.1016/j.carbon.2014.12.046.

[62] B. Mortazavi, A. V Shapeev, Anisotropic mechanical response, high negative thermal expansion, and outstanding dynamical stability of biphenylene monolayer revealed by machine-learning interatomic potentials, FlatChem 32 (2022), 100347.